

Article

# Montmorillonite-Synergized Water-Based Intumescent Flame Retardant Coating for Plywood

Xiaochun Hu, Zhao Sun, Xiaojun Zhu and Zhiqiang Sun \* 

School of Energy Science and Engineering, Central South University, Changsha 410083, China; xchu@csu.edu.cn (X.H.); zhaosun@csu.edu.cn (Z.S.); xjzhu@csu.edu.cn (X.Z.)

\* Correspondence: zqsun@csu.edu.cn

Received: 27 December 2019; Accepted: 24 January 2020; Published: 27 January 2020



**Abstract:** In this study, montmorillonite (MMT) was used as an inorganic synergist to prepare the water-based intumescent flame retardant (IFR) ornamental coating for plywood. Results indicate that the 7 wt.% MMT modified IFR coating (No. 3) possess the best fire resistance (longer than 20 min) of the tested samples according to the fire performance, which significantly declines the specific extinction area by  $44.12 \text{ m}^2 \cdot \text{kg}^{-1}$  compared to the coating without MMT by cone calorimeter. In addition, characterizations such as XPS, XRD, TG, SEM and FTIR were characterized to investigate the surface and bulk properties as well as the morphology of MMT synergized water-based IFR coating. It is revealed that the residual nitrogenous polyaromatic structure and 25.5% residual mass in the No. 3 coating are a result of the effect of MMT on the antioxidation properties of the char layer.

**Keywords:** montmorillonite; intumescent flame retardant coating; char layer; nitrogenous polyaromatic structure

## 1. Introduction

Wood has been widely used in production, construction, daily life and other activities for thousands of years due to its unique properties [1–3]. Unfortunately, the flammability of the wood can threaten the lives and properties of people, limiting its application [4,5]. Some researchers found that the fire retardancy of wood and wood-based panels can be improved by nanotechnology [6,7]. Specifically, a coating method can effectively inhibit the further spread of the fire and does not impose restrictions on the physical and mechanical properties of substrates [8–10]. One of them, water-based intumescent flame retardant (IFR) nanocoating, is more and more popular in the fireproof coating on wood. Moreover, water-based coating can lower the cost, reduce pollution, and improve the physical features of the building compared to solvent-based coating. IFR is also used in polypropylene and ethylene-propylene-diene rubber [11,12].

The composition of IFR coating adds various fire protection components to a binder, which mainly contains an acid source, carbon source, gas source, and fillers [13–16]. The coatings fuse, swell and carbonize to form the dense intumescent insulation char layer and also release nonflammable gas to dilute the flammable volatiles and oxygen in the flammable zone. The thickness of the char layer is much thicker than the coating, even up to hundreds of times, which has a valuable function in terms of the insulation of oxygen and heat. Meanwhile, the coating can also be decorative on the wood. Nevertheless, there are some defects to be improved to enhance its heat-shielding performance [17]. For example, the formation of char layer is oxidized with little hindrance over  $500 \text{ }^\circ\text{C}$  and the foam structure of the char layer is loose and uncompact [18]. To compensate for these faults, the appropriate filler is added to it to increase the flame resistance of char layer, especially in the middle and late stages, improving the strength, foam and fireproof performance of char layer. Filler, usually as a type of solid fine power, is insoluble in binder and solvent. However, the filler has poor coloring and covering,

but it can increase the thickness and solidity of the coating, enhancing the physical and chemical properties [19,20].

Montmorillonite (MMT) is the earthy mineral that consists of the negatively charged nanometer thickness silicate sheet layer stacked together by the electrostatic interaction between layers, while the structure cell in the crystalline structure is comprised of a layer of aluminum–oxygen octahedrons sandwiched between two layers of silicon–oxygen tetrahedrons. MMT has several modification possibilities and the expansion of application areas because it has the unique one-dimensional layered nanostructures and cation exchange properties. In comparison with sepiolite and halloysite, MMT has a kind of soft texture, resistance to acid and salt, thixotropy, and stability. Especially, the viscosity of coating can be enhanced by the addition of MMT. The synergic effect of MMT has been proven to increase fireproof performance. Organic, modified MMT was used as a nanofiller to enhance the fire protection, water and corrosion resistance of waterborne intumescent flame retardant coating [21]. The modified MMT was added to the polyurethane coating to increase compatibility [22]. The influence of organic, modified MMT on the optical transparency, thermal stability, fire retardant performances, and smoke suppression properties of the transparent fire-retardant coatings was investigated by different analytical instruments [23]. The polypropylene (PP)/IFR/Fe-MMT nanocomposites were prepared to investigate the effect of iron in the PP/IFR system [24]. Polyetheramines with ethyleneoxide/propyleneoxide were used to modify MMT and the polyol with the mixture of modified MMT possessed the intercalated/exfoliated structure [25].

In this study, a water-based IFR ornamental coating with waterborne acrylic resin and amino resin as the binder is designed to apply on the surface of the wood, possessing the remarkable fire prevention and smoke suppression performance. The IFR system in this coating is made up of the ammonium polyphosphate (APP), pentaerythritol (PER) and melamine (MEL). Besides, MMT is added to the coating to enhance the strength and fireproof performance of the IFR char layer [26]. In the present design, amino resin is not only a film-forming agent but also an excellent carbon-forming agent and a foaming agent. The film of the coating formed by acrylic resin is strong gloss, hardness and antistaining. Moreover, the amino resin and acrylic resin can promote the function of expansion and char forming, synergizing with the IFR system. Besides, the use of the MMT in the coating can increase the viscosity of the coating and have a synergistic effect with the IFR system, to improve the oxidation resistance of the char layer.

## 2. Materials and Methods

### 2.1. Materials

The amino resin (molecular formula:  $(C_3H_6N_6CH_2O)_x$ , molecular weight: 538.507) was provided from Hunan Xiangjiang Kansai Paint Co. LTD, Changsha, China. The acrylic resin (molecular formula:  $(C_3H_4O_2)_x$ ) was purchased from Zhongshan Langma Chemical Industry Co. LTD, Zhongshan, China. APP (type: HT-208, product name: APP200, effective content: 70%, pH: 5–7) was purchased from Jinan Taixing Fine Chemical Co. LTD, Jinan, China. PER (molecular formula:  $C_5H_{12}O_4$ , molecular weight: 136.15) and MEL (molecular formula:  $C_3H_6N_6$ , molecular weight: 126.12) were provided from College of Chemistry and Chemical Engineering, Central South University, Changsha, China. MMT (type: montmorillonite powder, product name: J-009, apparent viscosity: 20 mPa·s, whiteness: 85%, pH: 8–9, density:  $30\text{ g}\cdot\text{cm}^{-3}$ , CEC value: 80–100, average particle size: 1.9–2.3  $\mu\text{m}$ ) was purchased from Lingshou County Hengchang Mineral Products Processing Plant, Shijiazhuang, China. The MMT was characterized by XRD and TEM to analyze the phase composition and observe the microstructure as shown in Figure S1a,b, respectively. Table 1 shows the elemental composition of MMT. The scale crystal structure is the characteristic feature of the MMT primarily containing O, Si, and Al.

**Table 1.** Elemental composition of MMT from EDAX.

Element	O/k	Mg/k	Al/k	Si/k	K/k	Ca/k	Fe/k
Weight%	40.9	1.69	10.02	39.11	2.87	3.15	2.27
Atomic%	55.79	1.51	8.11	30.39	1.60	1.71	0.89
Error%	5.19	7.10	3.22	2.31	11.17	9.93	18.88

## 2.2. Preparation of Coatings

The APP, PER and MEL were ground by the agate grinding bowl and sieved through a sieve mesh (100 mesh, 0.15 mm) according to special proportion. The given acrylic resin and amino resin were added to the ground mixture to prepare the No. 0 coating that was adjusted to proper viscosity by adding a certain amount of deionized water as illustrated in Figure 1. Next, the No. 1, No. 2, No. 3 and No. 4 coatings were prepared by gradually adding a certain percentage of MMT to No. 0 coatings and mixed together with the ultrasonic assistance at 30 °C for 2 h. Table 2 shows the composition of all coatings, where there was no change except the content of MMT.

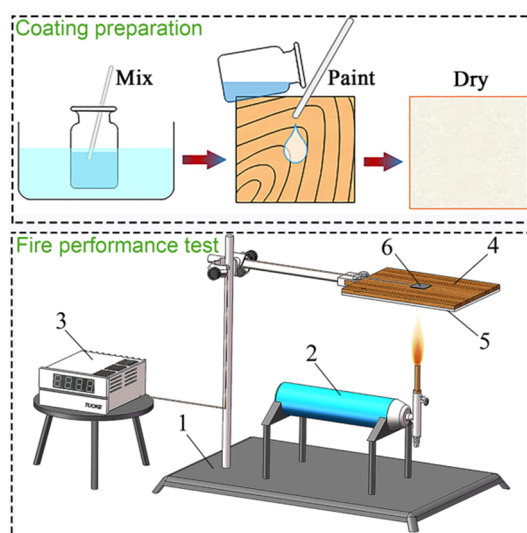


**Figure 1.** Schematic representation of nanocoating preparation and oriented structure, and the fire performance test setup: (1) test plywood; (2) thermocouple; (3) coating; (4) retort stand; (5) butane gas spray gun; (6) digital recorder.

**Table 2.** The composition of coatings.

Coating Name	Mass Percent/%				
	APP: MEL: PER (5:3:2)	Acrylic Resin	Amino Resin	MMT	Deionized Water
No. 0	50	7.5	7.5	0	35.0
No. 1	48.8	7.3	7.3	2.4	34.2
No. 2	47.6	7.1	7.1	4.8	33.4
No. 3	46.5	7.0	7.0	7.0	32.5
No. 4	45.5	6.8	6.8	9.1	31.8

## 2.3. Fire Performance Test

The insulating shield performance of each coating was conducted by the fire performance test as shown in Figure 1. First, the prepared coatings were weighted 20 g and applied on the commercial 3-layer plywood that was the size of 200 mm × 200 mm × 5 mm using a gloss rod as a roller, respectively, followed by drying in an indoor environment for 5 days. After the coating dried, the coated plywood was carried out by the fire performance test, where the sample was kept at a distance of 80 mm between

its lower surface and the burner nozzle. A K-type thermocouple was used to measure the surface temperature at the back of the plywood and the result was saved by the digital recorder. Besides, the temperature of the flame is all the time maintained at around 800 °C. During the test, the thickness of the coated plywood before burning and the thickness at the center part after burning were measured using the caliper. Thus, the thickness of the coating is equal to the thickness of the coated plywood minus the thickness of the plywood, and the thickness of the char layer is also equal to the coated plywood after fire performance test minus the thickness of the plywood.

#### 2.4. Combustion Test

The combustion test was accomplished utilizing cone calorimeter under the standard condition of ISO-5660-1. The No. 0 and No. 3 coatings were chosen to investigate the effect of MMT on the IFR coating according to the results of the fire performance test. The two coatings were applied on the 3-layer plywood with (100 mm × 100 mm × 5 mm). The resulting sample was dried in the indoor environment for 5 days before being tested horizontally in the cone and the distance between the cone bottom and the sample was 25 mm.

#### 2.5. Materials Characterization

Crystallinity and residual char layer were determined using a X-ray diffraction (XRD) (40 kV, 40 mA using a Cu K radiation source, Broker Corporation, Basel, The Switzerland). The XRD patterns were collected in the 2θ range from 5 to 90 with a step of 0.02° and 15 s counting time per angle. The chemical state of residual char layer after fire performance test was determined using X-ray photoelectron spectroscopy (XPS) (Thermo Fisher-VG Scientific, ESCALB250Xi, Waltham, MA, USA) under the following conditions: Source type: AL K Alpha, Spot size: 500 μm, Lens mode: standard. The molecule structure of the residual char layer was determined using the Perkin-Elmer 2000 FTIR (Perkin Elmer instruments, Basel, The Netherlands) with the char layer mixed with KBr. Morphology characterization and microstructure of char layer and MMT were conducted using Nova NanoSEM230 (FEI Electron Optics B.V, Czech Republic) at an acceleration voltage of 200 kV, and the element composition of MMT was examined using energy dispersive spectrometry (EDS). The char layer is divided into inner and outer parts to be tested.

### 3. Results and Discussion

The given line graph in Figure 2a reveals the heat insulation performance of the five coatings by fire performance tests. Overall, there is a rising trend for the fire resistance as the amounts of MMT is increased to add to IFR coating except for the excessive amounts of additions. Specifically, the fire resistance of No. 0 coating without MMT is about 10 min, while that of No. 1, No. 2 and No. 3 were 15 min and even more than 20 min, respectively as listed in Table 3. Furthermore, the thickness of the char layer ( $\delta_{cl}$ ) shows an upward trend, and then a downward with the MMT added to IFR.  $\delta_{cl}$  for No. 0, No. 1, No. 2, and No. 3 are 8.5 mm, 14.6 mm, 17.6 mm, and 19.2 mm but that of No. 4 drops to 15.0 mm in Table 3. This result is consistent with our hypothesis that the appropriate addition of MMT to IFR could enhance its heat insulation performance and promote the expansion of char layer.

**Table 3.** Fire resistant and combustion properties of IFR coatings.

Specimen	MMT wt. %	Fire Resistance/min	$\delta_{cl}/\text{mm}$	$\delta_{cl}/\text{mm}$	TTI/s	SEA/ $\text{m}^2 \cdot \text{kg}^{-1}$	TSR/ $\text{m}^2 \cdot \text{m}^{-2}$
No. 0	0	10	0.4	8.5	12.0	83.6	41.0
No. 1	2.4	15	0.4	14.6	-	-	-
No. 2	4.8	>20	0.4	17.6	-	-	-
No. 3	7.0	>20	0.4	19.2	14.0	39.5	21.2
No. 4	9.1	14	0.4	16.0	-	-	-

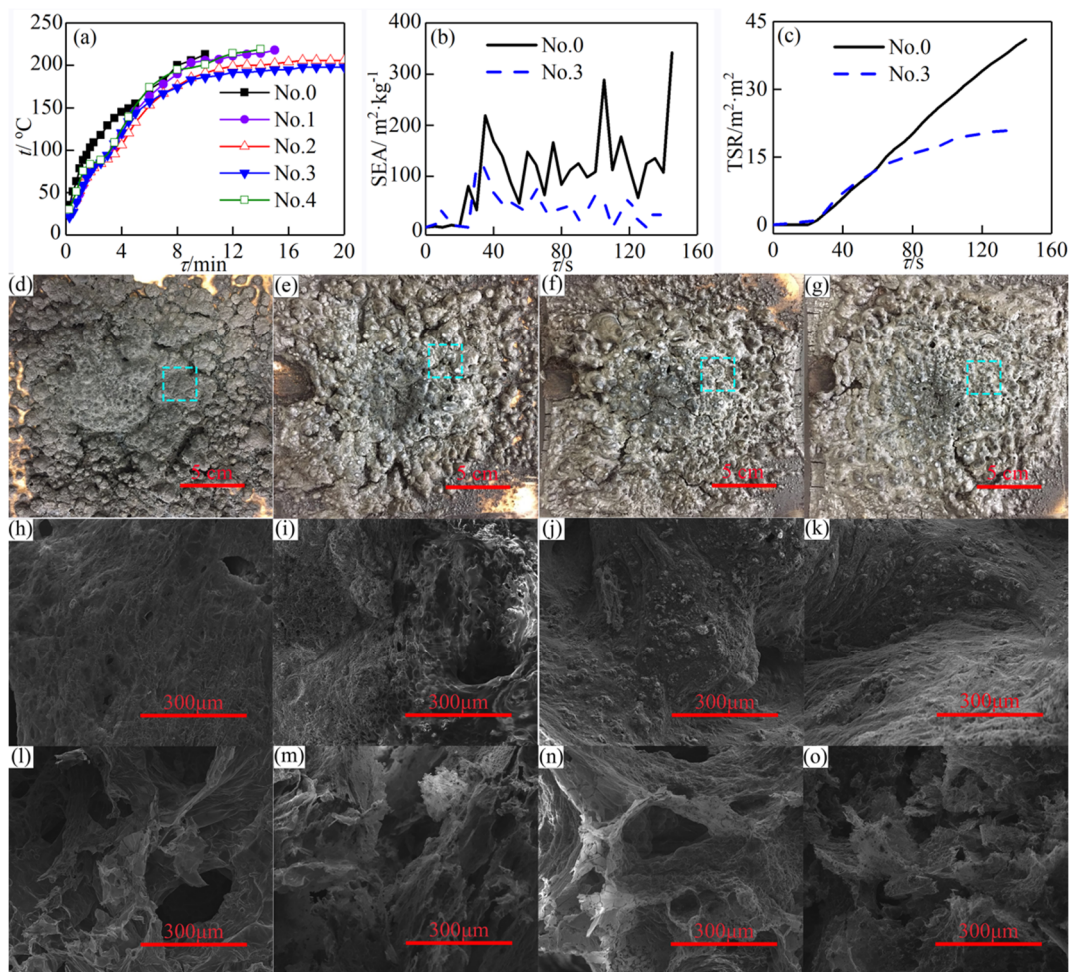


**Figure 2.** (a) The backside temperature curves of specimens, (b) SEA curves, (c) TSR curves. Images of char layers and the SEM images after fire performance test: (d) No. 0, (e) No. 2, (f) No. 3, and (g) No. 4. (h), (i), (j), and (k) are the outer images of No. 0, No. 2, No. 3, and No. 4, respectively; (l), (m), (n), and (o) are the inner images of No. 0, No. 2, No. 3, and No. 4, respectively.

Combustion performance of coatings is conducted using the cone test, providing combustion parameters such as time to ignition (TTI), specific extinction area (SEA), and total smoke release (TSR) and total smoke production (TSP). The TTI refers to the time from the heating of the material surface to the appearance of the continuous combustion of the surface under the present radiation intensity. The SEA is the ratio of the trimmed volume of flue gas to the mass loss rate of the sample. The TSR is the total heat release from the burning of the material to extinguishment of the flame under the present thermal radiation intensity. The difference between No. 0 and No. 3 coating are displayed in Table 3 and Figure 2b,c. Between No. 0 and No. 3, there was a slight increase in TTI from 12.00 s to 14.00 s, reflecting the coating with MMT was uneasy to ignite than the coating without MMT. Besides, the SEA is dramatically decreased with 7 wt.% MMT being added, and this figure of No. 3 declines  $44.12 \text{ m}^2 \cdot \text{kg}^{-1}$  compared to No. 0. SEA of No. 3 is also always lower than No. 0 from the beginning, as shown in Figure 2b. Similar to that trend, No. 2 see the TSR and TSP decreases sharply  $19.84 \text{ m}^2 \cdot \text{m}^{-2}$  and  $0.17 \text{ m}^2$ , respectively, in comparison with No. 0 in Figure 2c. It is unveiled that MMT can noticeably suppress the smoke release produced from IFR coating.

The appearance of char layers after the fire performance test are illustrated in Figure 2d–g. The No. 2–No. 4 char layers are more compact, and the rigidities are stronger than the No. 0 char layer. The SEM images of char layers are revealed in Figure 2h–o including the outer and the inner parts. The outer char layer of without MMT is flat in Figure 2h, while these outer char layers with MMT are

rough and coarse in Figure 2i–k. Note that there are some holes in the outer surface of No. 0, but the outer surface of No. 3, and No. 4 are still intact. Indeed, the strength of char layer was increased by the addition of MMT to IFR, capturing as much of the released gas as possible and curbing the transfer of heat to the plywood. In addition, there is some subtle difference between the inner char layer of No. 0 and these of No. 2, No. 3 and No. 4. The grain of No. 0 layer looks like “branch” and that of char layer with MMT is more like the “sponge” in Figure 2l–o. In summary, the morphological characteristics of char layer involving the outer and the inner are affected by the addition of MMT, which may be caused by the inorganic constituent interspersed on the char layer and the nanofiller dispersion.

The Figure 3 gives information on the recognized materials composition in char layers after the fire performance test. There were some diffraction peaks clearly in No. 3 outer and inner char layer in Figure 3a, respectively, corresponding to aluminum phosphate ( $\text{AlPO}_4$ ) and silicon phosphate ( $\text{SiP}_2\text{O}_7$ ), respectively. Thereinto, the  $\text{Si}_{2p}$  and  $\text{Al}_{2p}$  XPS spectrum are shown in Figure 3c,d. The broad scattering peaks were only observed in No. 0 char layer. The results represent the products from the interaction between MMT and APP alter the amorphous structure of the char layer. For example,  $\text{AlPO}_4$  can enhance the oxidization resistance of the outer char layer to maintain the integrity of the overall structure in No. 3. The amorphous char layer with the intumesce resulted from the  $\text{SiP}_2\text{O}_7$  in No. 3 inner char layer act as a vital role to decrease the thermal conductivity of the intumescent material. The FTIR spectra of materials are presented in Figure 3b and their wavelength ranges including  $3380\text{ cm}^{-1}$ , between  $1500$  and  $1600\text{ cm}^{-1}$ , between  $1000$  and  $1200\text{ cm}^{-1}$ ,  $790\text{ cm}^{-1}$  and  $670\text{ cm}^{-1}$ . The  $3380\text{ cm}^{-1}$  absorption band is responding to stretching vibration of N-H ( $\nu_{\text{N-H}}$ ) [27–30]. The characterized absorption peaks are observed in all samples. The stretching vibration of C=N ( $\nu_{\text{C=N}}$ ) between  $1500$  and  $1600\text{ cm}^{-1}$  [31–34] is observed in No. 0 and No. 3 char layers and No. 4 interior. However, the stretching vibration of the aromatic C=C ( $\nu_{\text{C=C}}$ ) is also found in No. 3 char layers. Similarly, the absorption bands approximately between  $670$  and  $790\text{ cm}^{-1}$  are corresponding to the bending vibration of the polyaromatic structures and external bending vibration of adjacent H on the aromatic ring, respectively. For every sample, it is to be noted that some broad bands are observed between  $1000$  and  $1200\text{ cm}^{-1}$ . These characteristic peaks are assigned to the phosphate groups [28,32,35]. The results are consistent with the XPS conclusion that the nitrogenous polyaromatic structures are prevented from decomposing to quaternary N species.

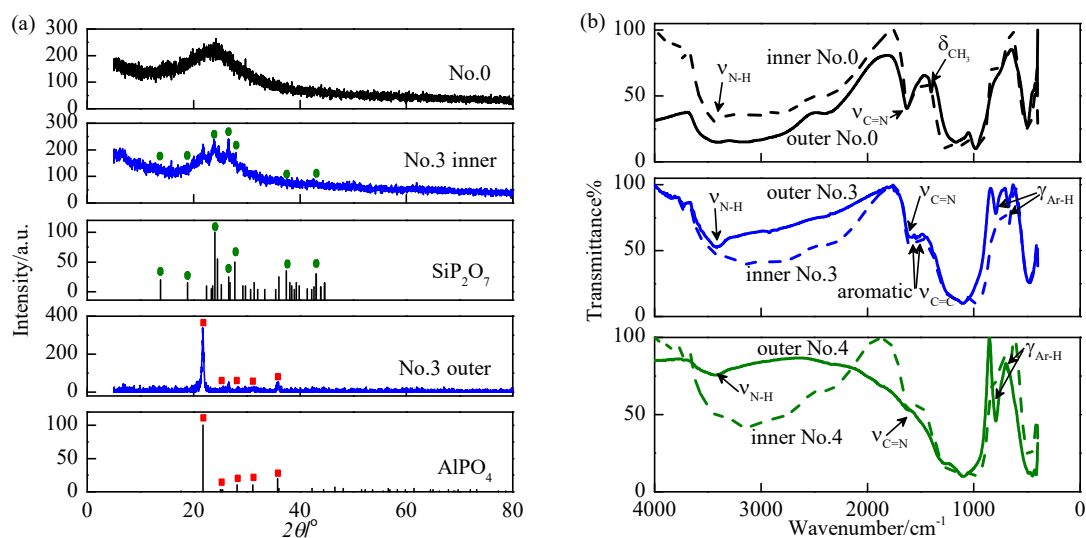
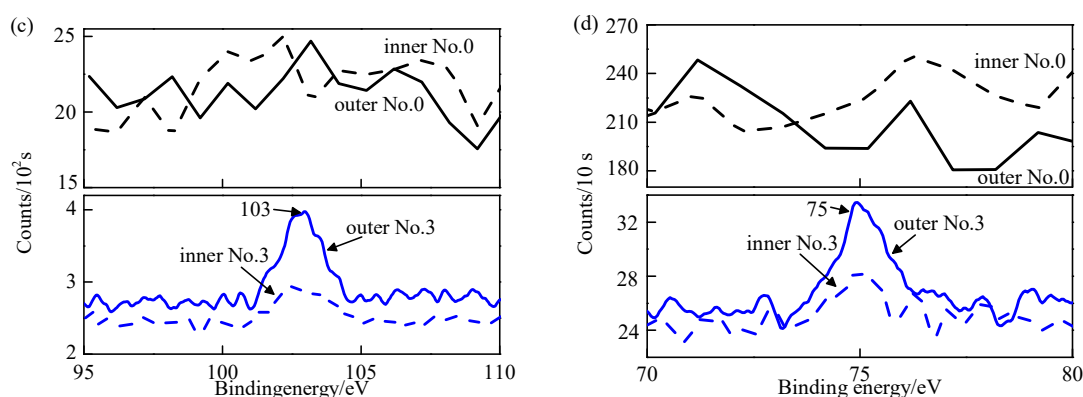
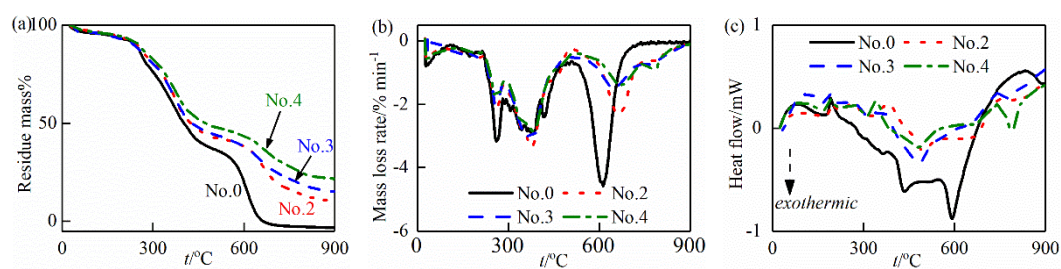


Figure 3. Cont.



**Figure 3.** (a) XRD patterns of char layers: SiP<sub>2</sub>O<sub>7</sub> (JCPDS 25-0755) and AlPO<sub>4</sub> (JCPDS 11-0500), (b) the FTIR spectra, (c) Si<sub>2p</sub> XPS spectrum and (d) Al<sub>2p</sub> XPS spectrum.

The TG, DTG, and DTA curves are illustrated in Figure 4a–c, respectively. The thermal decomposition process of coatings is divided into three stages including melting and softening (0–200 °C), intumescence and char layer formation (200–500 °C), and char layer degradation and loss (500–900 °C). At the first stage, the acrylic resin and amino resin start to soften and melt. Correspondingly, the distinct endothermic peak in the DTA curve is existed before 200 °C. Next, the coating is gradually carbonized into intumescent char layer. APP begins to decompose, generating phosphoric acid, pyrophosphate acid and releasing NH<sub>3</sub>. Afterward, the framework of char layer is initially formed by the esterification between PER and the (pyro)phosphoric acid and expands to form the porous char layer with the NH<sub>3</sub> and H<sub>2</sub>O released by MEL and MMT. The MMT affect this progress, where the trend is different between the No. 0 and the coatings added MMT (No. 1–No. 3) in DTA and DTG curves and the residual mass for No. 0 is 36.8% at 500 °C, and that of No. 3 is 44.4% (Table S1, Supporting Information). Finally, the char layer degrades with the loss of residual mass. As the addition of MMT to coating increase, the residual mass of char layer rise at 700 °C. For example, the residual mass of No. 0 is 0, while that of No. 3 remains 32.2%. Here, the MMT can improve the oxidation resistance of IFR char layer to delay the degradation.



**Figure 4.** The TG curves (a), DTG curves (b) and DTA curves (c) of No. 0, No. 2, No. 3, and No. 4 coatings.

Table 4 provides information about the main element content of char layers of No. 0 and No. 3 samples (Figure S1, Supporting Information). The content of C in outer char layer is higher than in inner for No. 0 and No. 3 while the other element contents (O, N, and P) in outer are lower than in the inner, which is the temperature difference between outer and inner. Moreover, the content of C in No. 3 added MMT is higher compared with No. 0 regardless of outer or inner. We can conclude that the addition MMT to IFR coating increases the degree of carbon accumulation and cross-linking of char layer. Meanwhile, the content of O in No. 3 outer is 0.86 times than that of No. 0 in Table 4. To be more precise, MMT also enhances the oxidization resistance of IFR char layer.

**Table 4.** Elemental composition of char layers.

Specimen	N <sub>1s</sub> %	C <sub>1s</sub> %	P <sub>2p</sub> %	O <sub>1s</sub> %	Si <sub>2p</sub> %	Al <sub>2p</sub> %
No. 0 outer	3.78	49.99	10.43	35.79	-	-
No. 0 inner	3.72	38.78	13.43	44.07	-	-
No. 3 outer	1.02	86.97	1.83	9.61	0.29	0.27
No. 3 inner	3.16	76.82	3.13	16.89	-	-

At each sample, there are two peaks of the O<sub>1s</sub> spectra with binding energies approximately 531.5 and 533 eV (Figure S2, Supporting Information). It is unachievable to identify the separate contributions of O<sub>1s</sub> band between inorganic and organic oxygen because of its lack of structure. The bands centered around 531.5 eV can be assigned to =O in phosphate and carbonyl groups. The bands centered at 533 eV can be assigned to –O– in C–O–C, C–O–P and/or C–OH groups [29–31]. The ratio of –O–/=O, according to the relative area percentages of functional groups, is shown versus outer and inner No. 0 and No. 3 in Table 5 [36]. Overall, it is to note that the ratio is always higher than one, and it is understood that the main species are the C–O–C and C–O–P bridge structures in comparison with the oxidized phosphate and carbonyl ones, whether the system without MMT or with it. Furthermore, the ratio of the outer surface is lower than the inner surface, and this is because the temperature of outer char layer is higher than the inner, preferentially oxidizing the outer char layer.

**Table 5.** The ratio of –O–/=O.

Sample	No. 0 Outer	No. 0 Inner	No. 3 Outer	No. 3 Inner
–O–/=O	1.74	1.80	3.03	4.20

Specifically, the –O–/=O ratio dramatically raises when the sample is added MMT. From No. 0 to No. 3, the ratios increase 1.29 (outer surface) and 2.40 (inner surface), respectively. There is a tendency to believe that the MMT can handicap the oxidation of the char layer. For the P<sub>2p</sub> spectra (Figure S3, Supporting Information), the binding energies observed between 134 and 135 eV are corresponding to phosphate species and P<sub>2</sub>O<sub>5</sub> [24]. The content of P<sub>2p</sub> in the outer surface is lower than inner surface in No. 0 and No. 3, reflecting the P in outer surface is easy oxidized to volatilize by forming the P<sub>2</sub>O<sub>5</sub>. In addition, the content of P in No. 0 is higher than No. 3 regardless of the outer surface and the inner surface.

For all samples of the C<sub>1s</sub> spectra (Figure S4, Supporting Information), the numbers and positions of the peaks are the same. The peaks at about 284.6 eV assign to C–H and C–C in aliphatic and aromatic species in the char layer [37]. The bands around 285.8 eV are the contributions of C=N in heterocyclic compounds [38–40]. The nitrogenous polyaromatic structure is observed in four samples, but the skeleton structure is mainly composed of the aromatic C and C–C. Unfortunately, it is difficult to distinguish the aromatic C and aliphatic C using the XPS. No. 0 samples give rise to a single N<sub>1s</sub> peak, but No. 3 samples emerge single broad peak and double peak in Figure 5. The N<sub>1s</sub> spectra can be assumed three typical peaks at 398.3 eV 400.6 eV (for the sample with MMT) and 401 eV (for the sample without MMT). These two bands at about 398.3 eV and 400.6 eV assign to pyridinic groups and pyrrolic nitrogen, respectively [41–44]. The 401 eV is corresponding to the quaternary N. In general, Nitrogenous polyaromatic structures, such as pyridinic and pyrrolic N, are oxidized to quaternary N as the temperature rises. There are still the pyridinic and pyrrolic N in the No. 3 char layer but No. 0 only contains the quaternary N, revealing that the MMT can restrain the degradation of the polyaromatic structures.

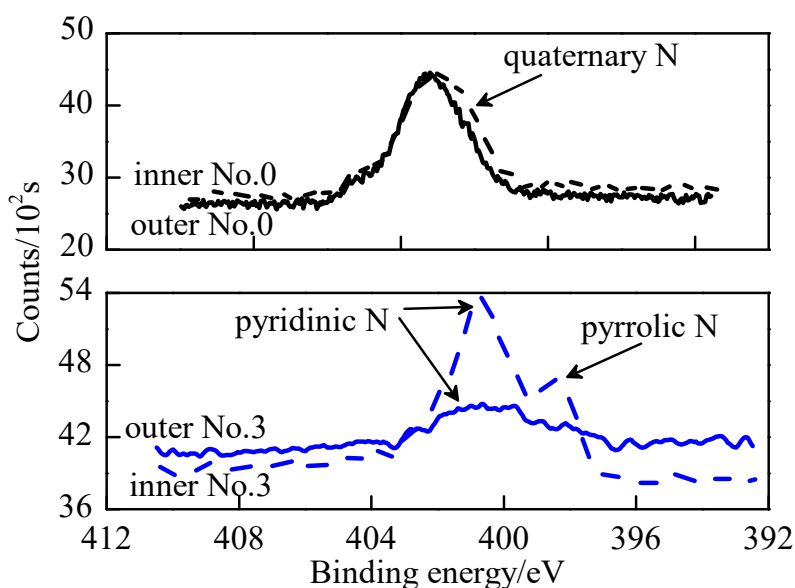


Figure 5. The  $N_{1s}$  XPS spectrum.

Overall, the amorphous char layer is composed of nitrogenous polyaromatic skeleton structure and bridge structure. The addition of 7 wt.% MMT to IFR coating restrains the decomposition of the nitrogenous polyaromatic structure of the char layer to improve the oxidation resistance of the char layer and increase the residual mass of char layer at 700 °C. Moreover, the  $-O/=O$  ratios of the No. 3 sample are significantly increased regardless of the outer or inner than No. 0.

#### 4. Conclusions

In summary, we innovatively demonstrated the preparation of novel water-based IFR coating with MMT through a layer-by-layer method on plywood. The fire resistance, smoke suppression, and oxidation resistance of the coating was increased corresponding to the addition of MMT into it. For example, the addition of 7 wt.% MMT to the IFR coating was found to prolong the fire resistance of the No. 3 coating (more than 20 min) than the No. 0 coating (10 min); the smoke suppression of the coating increased dramatically: the SEA of No. 3 coating decreases by 44.12  $m^2 \cdot kg^{-1}$  than that of No. 0; the oxidation resistance of the coating was also enhanced since the ratio of  $-O/=O$  for No. 3 grew significantly and the residual mass increased to 25.5% at 700 °C. In addition, the formation of nitrogenated aromatic species in the char layer was protected by the addition of MMT to the IFR coating, which was shown by the morphological change of the char layer at both the micron and centimeter level.

**Supplementary Materials:** The following are available online at <http://www.mdpi.com/2079-6412/10/2/109/s1>, Figure S1: (a) The XRD pattern of MMT and (b) SEM image of MMT.; Figure S2: The composition of element for No.0 and No.3 outer and inner char layers; Figure S3: The O1s XPS spectrum: (a) outer No.0; (b) inner No.0; (c) outer No.3; and (d) inner No.3; Figure S4: The P2p XPS spectrum; Figure S5: The C1s XPS spectrum: (a) outer No.0; (b) inner No.0; (c) outer No.3; and (d) innerNo.3. Table S1: Residual mass of coatings at different temperature.

**Author Contributions:** Conceptualization, X.H. and Z.S.; methodology, X.H.; software, X.H.; writing—original draft preparation, X.H.; writing—review and editing, Z.S., X.Z., and Z.S.; supervision, Z.S.; project administration, Z.S.; funding acquisition, Z.S. All authors have read and agreed to the published version of the manuscript.

**Funding:** This research was funded by the National Natural Science Foundation of China, grant number 51876224, the Hunan Provincial Natural Science Foundation of China, grant number 2017JJ1031, and the Innovation-Driven Project of Central South University, grant number 2020CX008.

**Conflicts of Interest:** The authors declare no conflict of interest.

## Abbreviations

APP	ammonium polyphosphate
DTA	differential thermal analysis
FTIR	Fourier transform infrared spectroscopy
IFR	intumescent flame retardant
MEL	melamine
MMT	montmorillonite
PER	pentaerythritol
SEA	specific extinction area
SEM	SEM
TG	thermogravimetry
TSP	total smoke production
TSR	total smoke release
TTI	time to ignition
XPS	X-ray photoelectron spectroscopy
XRD	X-ray diffraction

## Nomenclature

$\delta_{cl}$	Thickness of char layer
$\delta_{ct}$	Thickness of coating
$t$	Temperature
$t_{cw}$	Surface temperature at the back of coated wood
$\tau$	time

## References

- Carosio, F.; Cuttica, F.; Medina, L.; Berglund, L.A. Clay nanopaper as multifunctional brick and mortar fire protection coating—wood case study. *Mater. Des.* **2016**, *93*, 357–363. [\[CrossRef\]](#)
- Gan, W.; Chen, C.; Wang, Z.; Song, J.; Kuang, Y.; He, S.; Mi, R.; Sunderland, P.B.; Hu, L. Dense, self-formed char layer enables a fire-retardant wood structural material. *Adv. Funct. Mater.* **2019**, *29*, 1807444. [\[CrossRef\]](#)
- Yan, L.; Xu, Z.; Liu, D. Synthesis and application of novel magnesium phosphate ester flame retardants for transparent intumescent fire-retardant coatings applied on wood substrates. *Prog. Org. Coat.* **2019**, *129*, 327–337. [\[CrossRef\]](#)
- Davis, R.; Li, Y.-C.; Gervasio, M.; Luu, J.; Kim, Y.S. One-pot, bioinspired coatings to reduce the flammability of flexible polyurethane foams. *ACS Appl. Mater. Interfaces* **2015**, *7*, 6082–6092. [\[CrossRef\]](#)
- Guo, H.; Luković, M.; Mendoza, M.; Schlepütz, C.M.; Griffa, M.; Xu, B.; Gaan, S.; Herrmann, H.; Burgert, I. Bioinspired struvite mineralization for fire-resistant wood. *ACS Appl. Mater. Interfaces* **2019**, *11*, 5427–5434. [\[CrossRef\]](#)
- Papadopoulos, A.N.; Taghiyari, H.R. Innovative wood surface treatments based on nanotechnology. *Coatings* **2019**, *9*, 866. [\[CrossRef\]](#)
- Papadopoulos, A.N.; Bikiaris, D.N.; Mitropoulos, A.C.; Kyzas, G.Z. Nanomaterials and chemical modifications for enhanced key wood properties: A review. *Nanomaterials* **2019**, *9*, 607. [\[CrossRef\]](#)
- Laachachi, A.; Ball, V.; Apaydin, K.; Toniazzo, V.; Ruch, D. Diffusion of polyphosphates into (poly (allylamine)-montmorillonite) multilayer films: Flame retardant-intumescent films with improved oxygen barrier. *Langmuir* **2011**, *27*, 13879–13887. [\[CrossRef\]](#)
- Xie, W.; Chen, H.; He, D.; Zhang, Y.; Fu, L.; Ouyang, J.; Yang, H. An emerging mineral-based composite flame retardant coating: Preparation and enhanced fireproof performance. *Surf. Coat. Technol.* **2019**, *367*, 118–126. [\[CrossRef\]](#)
- Huang, Y.; Jiang, S.; Liang, R.; Liao, Z.; You, G. A green highly-effective surface flame-retardant strategy for rigid polyurethane foam: Transforming uv-cured coating into intumescent self-extinguishing layer. *Compos. Part A Appl. Sci. Manuf.* **2019**, *125*, 105534. [\[CrossRef\]](#)
- Chen, H.; Wang, J.; Ni, A.; Ding, A.; Han, X.; Sun, Z. The effects of a macromolecular charring agent with gas phase and condense phase synergistic flame retardant capability on the properties of pp/ifr composites. *Materials* **2018**, *11*, 111. [\[CrossRef\]](#) [\[PubMed\]](#)

12. Wang, J.; Xue, L.; Zhao, B.; Lin, G.; Jin, X.; Liu, D.; Zhu, H.; Yang, J.; Shang, K. Flame retardancy, fire behavior, and flame retardant mechanism of intumescent flame retardant epdm containing ammonium polyphosphate/pentaerythritol and expandable graphite. *Materials* **2019**, *12*, 4035. [[CrossRef](#)] [[PubMed](#)]
13. Kaur, J.; Ahmad, F.; Ullah, S.; Yusoff, P.M.; Ahmad, R. The role of bentonite clay on improvement in char adhesion of intumescent fire-retardant coating with steel substrate. *Arab. J. Sci. Eng.* **2017**, *42*, 2043–2053. [[CrossRef](#)]
14. Puri, R.G.; Khanna, A. Intumescent coatings: A review on recent progress. *J. Coat. Technol. Res.* **2017**, *14*, 1–20. [[CrossRef](#)]
15. Li, X.-L.; Zhang, F.-H.; Jian, R.-K.; Ai, Y.-F.; Ma, J.-L.; Hui, G.-J.; Wang, D.-Y. Influence of eco-friendly calcium gluconate on the intumescent flame-retardant epoxy resin: Flame retardancy, smoke suppression and mechanical properties. *Compos. Part B Eng.* **2019**, *176*, 107200. [[CrossRef](#)]
16. Yang, B.; Chen, Y.; Zhang, M.; Yuan, G. Synergistic and compatibilizing effect of octavinyl polyhedral oligomeric silsesquioxane nanoparticles in polypropylene/intumescent flame retardant composite system. *Compos. Part A Appl. Sci. Manuf.* **2019**, *123*, 46–58. [[CrossRef](#)]
17. Ahmad, F.; Zulkurnain, E.S.; Ullah, S.; Amir, N. Effects of nano-sized boron nitride on thermal decomposition and water resistance behaviour of epoxy-based intumescent coating. *J. Anal. Appl. Pyrolysis* **2018**, *132*, 171–183. [[CrossRef](#)]
18. Hu, X.; Zhu, X.; Sun, Z. Effect of caalco3-ldhs on fire resistant properties of intumescent fireproof coatings for steel structure. *Appl. Surf. Sci.* **2018**, *457*, 164–169. [[CrossRef](#)]
19. Li, Z.; Wang, D.-Y. Nano-architected mesoporous silica decorated with ultrafine co3o4 toward an efficient way to delaying ignition and improving fire retardancy of polystyrene. *Mater. Des.* **2017**, *129*, 69–81. [[CrossRef](#)]
20. Kim, N.; Bhattacharyya, D. Development of fire resistant wool polymer composites: Mechanical performance and fire simulation with design perspectives. *Mater. Des.* **2016**, *106*, 391–403. [[CrossRef](#)]
21. Wang, J.; Wang, G. Influences of montmorillonite on fire protection, water and corrosion resistance of waterborne intumescent fire retardant coating for steel structure. *Surf. Coat. Technol.* **2014**, *239*, 177–184. [[CrossRef](#)]
22. Hassan, M.; Kozlowski, R.; Obidzinski, B. New fire-protective intumescent coatings for wood. *J. Appl. Polym. Sci.* **2008**, *110*, 83–90. [[CrossRef](#)]
23. Yan, L.; Xu, Z.; Wang, X. Synergistic effects of organically modified montmorillonite on the flame-retardant and smoke suppression properties of transparent intumescent fire-retardant coatings. *Prog. Org. Coat.* **2018**, *122*, 107–118. [[CrossRef](#)]
24. Liu, H.; Zhong, Q.; Kong, Q.; Zhang, X.; Li, Y.; Zhang, J. Synergistic effect of organophilic fe-montmorillonite on flammability in polypropylene/intumescent flame retardant system. *J. Therm. Anal. Calorim.* **2014**, *117*, 693–699. [[CrossRef](#)]
25. Indennitate, L.; Cannoletta, D.; Lionetto, F.; Greco, A.; Maffezzoli, A. Nanofilled polyols for viscoelastic polyurethane foams. *Polym. Int.* **2010**, *59*, 486–491. [[CrossRef](#)]
26. Lim, K.-S.; Bee, S.-T.; Sin, L.T.; Tee, T.-T.; Ratnam, C.; Hui, D.; Rahmat, A. A review of application of ammonium polyphosphate as intumescent flame retardant in thermoplastic composites. *Compos. Part B Eng.* **2016**, *84*, 155–174. [[CrossRef](#)]
27. Kim, H.; Kim, D.W.; Vasagar, V.; Ha, H.; Nazarenko, S.; Ellison, C.J. Polydopamine-graphene oxide flame retardant nanocoatings applied via an aqueous liquid crystalline scaffold. *Adv. Funct. Mater.* **2018**, *28*, 1803172. [[CrossRef](#)]
28. Jiang, Z.; Li, H.; He, Y.; Liu, Y.; Dong, C.; Zhu, P. Flame retardancy and thermal behavior of cotton fabrics based on a novel phosphorus-containing siloxane. *Appl. Surf. Sci.* **2019**, *479*, 765–775. [[CrossRef](#)]
29. Hu, X.; Zhu, X.; Sun, Z. Efficient flame-retardant and smoke-suppression properties of mgalco3-ldhs on the intumescent fire retardant coating for steel structures. *Prog. Org. Coat.* **2019**, *135*, 291–298. [[CrossRef](#)]
30. Wu, N.; Fu, G.; Yang, Y.; Xia, M.; Yun, H.; Wang, Q. Fire safety enhancement of a highly efficient flame retardant poly (phenylphosphoryl phenylenediamine) in biodegradable poly (lactic acid). *J. Hazard. Mater.* **2019**, *363*, 1–9. [[CrossRef](#)]
31. Xu, J.; Shen, K.; Xue, B.; Li, Y.-X. Microporous carbon nitride as an effective solid base catalyst for knoevenagel condensation reactions. *J. Mol. Catal. A Chem.* **2013**, *372*, 105–113. [[CrossRef](#)]

32. Cheng, J.; Wang, J.; Yang, S.; Zhang, Q.; Huo, S.; Zhang, Q.; Hu, Y.; Ding, G. Benzimidazolyl-substituted cyclotriphosphazene derivative as latent flame-retardant curing agent for one-component epoxy resin system with excellent comprehensive performance. *Compos. Part B Eng.* **2019**, *177*, 107440. [[CrossRef](#)]
33. Qiu, S.; Zou, B.; Sheng, H.; Guo, W.; Wang, J.; Zhao, Y.; Wang, W.; Yuen, R.K.; Kan, Y.; Hu, Y. Electrochemically exfoliated functionalized black phosphorene and its polyurethane acrylate nanocomposites: Synthesis and applications. *Acs Appl. Mater. Interfaces* **2019**, *11*, 13652–13664. [[CrossRef](#)] [[PubMed](#)]
34. Jian, R.-K.; Ai, Y.-F.; Xia, L.; Zhao, L.-J.; Zhao, H.-B. Single component phosphamide-based intumescent flame retardant with potential reactivity towards low flammability and smoke epoxy resins. *J. Hazard. Mater.* **2019**, *371*, 529–539. [[CrossRef](#)] [[PubMed](#)]
35. Liu, Y.; Wang, Q.-Q.; Jiang, Z.-M.; Zhang, C.-J.; Li, Z.-F.; Chen, H.-Q.; Zhu, P. Effect of chitosan on the fire retardancy and thermal degradation properties of coated cotton fabrics with sodium phytate and aptes by lbl assembly. *J. Anal. Appl. Pyrolysis* **2018**, *135*, 289–298. [[CrossRef](#)]
36. Lionetto, F.; López-Muñoz, R.; Espinoza-González, C.; Mis-Fernández, R.; Rodríguez-Fernández, O.; Maffezzoli, A. A study on exfoliation of expanded graphite stacks in candelilla wax. *Materials* **2019**, *12*, 2530. [[CrossRef](#)] [[PubMed](#)]
37. Cai, W.; Guo, W.; Pan, Y.; Wang, J.; Mu, X.; Feng, X.; Yuan, B.; Wang, B.; Hu, Y. Polydopamine-bridged synthesis of ternary h-bn@pda@sno2 as nanoenhancers for flame retardant and smoke suppression of epoxy composites. *Compos. Part A Appl. Sci. Manuf.* **2018**, *111*, 94–105. [[CrossRef](#)]
38. Bourbigot, S.; Le Bras, M.; Delobel, R.; Gengembre, L. Xps study of an intumescent coating: Ii. Application to the ammonium polyphosphate/pentaerythritol/ethylenic terpolymer fire retardant system with and without synergistic agent. *Appl. Surf. Sci.* **1997**, *120*, 15–29. [[CrossRef](#)]
39. Mane, G.P.; Talapaneni, S.N.; Lakhi, K.S.; Ilbeygi, H.; Ravon, U.; Al-Bahily, K.; Mori, T.; Park, D.H.; Vinu, A. Highly ordered nitrogen-rich mesoporous carbon nitrides and their superior performance for sensing and photocatalytic hydrogen generation. *Angew. Chem. Int. Ed.* **2017**, *56*, 8481–8485. [[CrossRef](#)]
40. Zhang, Y.; Bo, X.; Nsabimana, A.; Luhana, C.; Wang, G.; Wang, H.; Li, M.; Guo, L. Fabrication of 2d ordered mesoporous carbon nitride and its use as electrochemical sensing platform for h2o2, nitrobenzene, and nadh detection. *Biosens. Bioelectron.* **2014**, *53*, 250–256. [[CrossRef](#)]
41. Bourbigot, S.; Le Bras, M.; Gengembre, L.; Delobel, R. Xps study of an intumescent coating application to the ammonium polyphosphate/pentaerythritol fire-retardant system. *Appl. Surf. Sci.* **1994**, *81*, 299–307. [[CrossRef](#)]
42. Li, Q.; Yang, J.; Feng, D.; Wu, Z.; Wu, Q.; Park, S.S.; Ha, C.-S.; Zhao, D. Facile synthesis of porous carbon nitride spheres with hierarchical three-dimensional mesostructures for co 2 capture. *Nano Res.* **2010**, *3*, 632–642. [[CrossRef](#)]
43. Sheng, Z.-H.; Shao, L.; Chen, J.-J.; Bao, W.-J.; Wang, F.-B.; Xia, X.-H. Catalyst-free synthesis of nitrogen-doped graphene via thermal annealing graphite oxide with melamine and its excellent electrocatalysis. *Acs Nano* **2011**, *5*, 4350–4358. [[CrossRef](#)] [[PubMed](#)]
44. Jin, X.; Sun, J.; Zhang, J.S.; Gu, X.; Bourbigot, S.; Li, H.; Tang, W.; Zhang, S. Preparation of a novel intumescent flame retardant based on supramolecular interactions and its application in polyamide 11. *Acs Appl. Mater. Interfaces* **2017**, *9*, 24964–24975. [[CrossRef](#)]

